

UC Davis

UC Davis Previously Published Works

Title

When machine vision meets histology: A comparative evaluation of model architecture for classification of histology sections

Permalink

<https://escholarship.org/uc/item/9kf5g23x>

Authors

Zhong, Cheng

Han, Ju

Borowsky, Alexander

et al.

Publication Date

2017

DOI

10.1016/j.media.2016.08.010

Peer reviewed

# When Machine Vision Meets Histology: A Comparative Evaluation of Model Architecture for Classification of Histology Sections

Cheng Zhong<sup>1</sup>, Ju Han<sup>1</sup>, Alexander Borowsky<sup>3</sup>, Yunfu Wang<sup>1,4</sup>, Bahram Parvin<sup>2</sup>, Hang Chang<sup>1,\*</sup>

<sup>1</sup>*Lawrence Berkeley National Laboratory, Berkeley, CA, USA*

<sup>2</sup>*Department of Electrical and Biomedical Engineering, University of Nevada, Reno, NV, USA*

<sup>3</sup>*Center for Comparative Medicine, University of California, Davis, CA, USA*

<sup>4</sup>*Department of Neurology, Taihe Hospital, Hubei University of Medicine, Shiyan, Hubei, China*

\* *Corresponding Author: hchang@lbl.gov*

---

## Abstract

Classification of histology sections in large cohorts, in terms of distinct regions of microanatomy (e.g., stromal) and histopathology (e.g., tumor, necrosis), enables the quantification of tumor composition, and the construction of predictive models of genomics and clinical outcome. To tackle the large technical variations and biological heterogeneities, which are intrinsic in large cohorts, emerging systems utilize either prior knowledge from pathologists or unsupervised feature learning for invariant representation of the underlying properties in the data. However, to a large degree, the architecture for tissue histology classification remains unexplored and requires urgent systematical investigation. This paper is the first attempt to provide insights into three fundamental questions in tissue histology classification: I. Is unsupervised feature learning preferable to human engineered features? II. Does cellular saliency help? III. Does the sparse feature encoder contribute to recognition? We show that (a) in I, both Cellular Morphometric Feature and features from unsupervised feature learning lead to superior performance when compared to SIFT and [Color, Texture]; (b) in II, cellular saliency incorporation impairs the performance for systems built upon pixel-/patch-level features; and (c) in III, the effect of the sparse feature encoder is correlated with the robustness of features, and the performance can be consistently improved by the multi-stage extension of systems built upon both Cellular Morphometric Feature and features from unsupervised feature learning. These insights are validated with two cohorts of Glioblastoma Multiforme (GBM) and Kidney Clear Cell Car-

cinoma (KIRC).

*Keywords:* Computational Histopathology, Classification, Unsupervised Feature Learning, Sparse Feature Encoder

---

## 1. Introduction

Although molecular characterization of tumors through gene expression analysis has become a standardized technique, bulk tumor gene expression data provide only an average genome-wide measurement for a biopsy and fail to reveal inherent cellular composition and heterogeneity of a tumor. On the other hand, histology sections provide wealth of information about the tissue architecture that contains multiple cell types at different states of cell cycles. These sections are often stained with hematoxylin and eosin (H&E) stains, which label DNA (e.g., nuclei) and protein contents, respectively, in various shades of color. Furthermore, morphometric aberrations in tumor architecture often lead to disease progression, and it is therefore desirable to quantify tumor architecture as well as the corresponding morphometric aberrations in large cohorts for the construction of predictive models of end points, e.g., clinical outcome, which have the potential for improved diagnosis and therapy.

Despite the efforts by some researchers on reducing inter- and intra-pathologist variations [Dalton et al. \(2000\)](#) during manual analysis, this approach is not a scalable solution, and therefore impedes the effective representation and recognition from large cohorts for scientific discoveries. With its value resting on capturing detailed morphometric signatures and organization, automatic quantitative analysis of a large collection of histological data is highly desirable, and is unfortunately impaired by a number of barriers mostly originating from the technical variations (e.g., fixation, staining) and biological heterogeneities (e.g., cell type, cell state) always presented in the data. Specifically, a histological tissue section refers to an image of a thin slice of tissue applied to a microscopic slide and scanned from a light microscope, and the technical variations and biological heterogeneities lead to significant color variations both within and across tissue sections. For example, within the same tissue section, nuclear signal (color) varies from light blue to dark blue due to the variations of their chromatin content; and nuclear intensity in one tissue section may be very close to the background intensity (e.g., cytoplasmic, macromolecular components) in another tissue section.

It is also worth to mention that alternative staining (e.g., fluorescence) and microscopy methods (multi-spectral imaging) have been proposed and studied in or-

33 der to overcome the fundamental limitations/challenges in tissue histology [Stack](#)  
34 [et al. \(2014\)](#); [Levenson et al. \(2015\)](#); [Rimm \(2014\)](#); [Huang et al. \(2013\)](#); [Ghaznavi](#)  
35 [et al. \(2013\)](#); however, H&E stained tissue sections are still the gold standard for  
36 the assessment of tissue neoplasm. Furthermore, the efficient and effective rep-  
37 resentation and interpretation of H&E tissue histology sections in large cohorts  
38 (e.g., The Cancer Genome Atlas dataset) have the potential to provide predictive  
39 models of genomics and clinical outcome, and are therefore urgently required.

40 Although many techniques have been designed and developed for tissue histol-  
41 ogy classification (see Section 2), the architecture for tissue histology classifica-  
42 tion remains largely unexplored and requires urgent systematical investigation. To  
43 fulfil this goal, our paper provides insights to three fundamental questions in tissue  
44 histology classification: I. Is unsupervised feature learning preferable to human  
45 engineered features? II. Does cellular prior knowledge help? III. Does the sparse  
46 feature encoder contribute to recognition? The novelty of our work resides in three  
47 folds: (i) architecture design: we have systematically experimented the system ar-  
48 chitecture with various combinations of feature types, feature extraction strategies  
49 and intermediate layers based on sparsity/locality-constrained feature encoders,  
50 which ensures the extensive evaluation and detailed insights on impact of the key  
51 components during the architecture construction; (ii) experimental design: our  
52 experimental evaluation has been performed through cross-validation on two in-  
53 dependent datasets with distinct tumor types, where both datasets have been cu-  
54 rated by our pathologist to provide examples of distinct regions of microanatomy  
55 (e.g., stromal) and histopathology (e.g., tumor, necrosis) with sufficient amount  
56 of technical variations and biological heterogeneities, so that the architecture can  
57 be faithfully tested and validated against important topics in histopathology (see  
58 Section 4 for details). More importantly, such an experimental design (combina-  
59 tion of cross-validation and validation on independent datasets), to the maximum  
60 extent, ensures the consistency and unbiasedness of our findings; and (iii) out-  
61 come: the major outcome of our work are well-justified insights in the architec-  
62 ture design/construction. Specifically, we suggest that the sparse feature encoders  
63 based on Cellular Morphometric Feature and features from unsupervised feature  
64 learning provide the best configurations for tissue histology classification. Fur-  
65 thermore, these insights also led to the construction of a highly scalable and ef-  
66 fective system (**CMF-PredictiveSFE-KSPM**, see Section 4 for details) for tissue  
67 histology classification. Finally, we believe that our work will not only benefit the  
68 research in computational histopathology, but will also benefit the community of  
69 medical image analysis at large by shedding lights on the systematical study of  
70 other important topics.

71 Organization of this paper is as follows: Section 2 reviews related works. Sec-  
72 tion 3 describes various components for the system architecture during evaluation.  
73 Section 4 elaborates the details of our experimental setup, followed by a detailed  
74 discussion on the experimental results. Lastly, section 5 concludes the paper.

## 75 **2. Related Work**

76 Current work on histology section analysis is typically formulated and per-  
77 formed at multiple scales for various end points, and several outstanding reviews  
78 can be found in [Demir and Yener \(2009\)](#); [Gurcan et al. \(2009\)](#). From our perspec-  
79 tive, the trends are: (i) nuclear segmentation and organization for tumor grading  
80 and/or the prediction of tumor recurrence [Basavanhally et al. \(2009\)](#); [Doyle et al.](#)  
81 [\(2011\)](#).(ii) patch level analysis (e.g., small regions) [Bhagavatula et al. \(2010\)](#);  
82 [Kong et al. \(2010\)](#), using color and texture features, for tumor representation. and  
83 (iii) detection and representation of the auto-immune response as a prognostic tool  
84 for cancer [Fatakdawala et al. \(2010\)](#).

85 While our focus is on the classification of histology sections in large cohorts,  
86 in terms of distinct regions of microanatomy (e.g., stromal) and histopathology  
87 (e.g., tumor, necrosis), the major challenge resides in the large amounts of tech-  
88 nical variations and biological heterogeneities in the data [Kothari et al. \(2012\)](#),  
89 which typically leads to techniques that are tumor type specific or even laboratory  
90 specific. The major efforts addressing this issue fall into two distinct categories:  
91 (i) fine-tuning human engineered features [Bhagavatula et al. \(2010\)](#); [Kong et al.](#)  
92 [\(2010\)](#); [Kothari et al. \(2012\)](#); [Chang et al. \(2013a\)](#); and (ii) applying automatic fea-  
93 ture learning [Huang et al. \(2011\)](#); [Chang et al. \(2013c\)](#) for robust representation.  
94 Specifically, the authors in [Bhagavatula et al. \(2010\)](#) designed multi-scale image  
95 features to mimic the visual cues that experts utilized for the automatic identifi-  
96 cation and delineation of germ-layer components in H&E stained tissue histology  
97 sections of teratomas derived from human and nonhuman primate embryonic stem  
98 cells; the authors in [Kong et al. \(2010\)](#) integrated multiple texture features (e.g.,  
99 wavelet features) into a texture-based content retrieval framework for the identi-  
100 fication of tissue regions that inform diagnosis; the work in [Kothari et al. \(2012\)](#)  
101 utilized various features (e.g., color, texture and shape) for the study of visual  
102 morphometric patterns across tissue histology sections; and the work in [Chang](#)  
103 [et al. \(2013a\)](#) constructed the cellular morphometric context based on various  
104 cellular morphometric features for effective representation and classification of  
105 distinct regions of microanatomy and histopathology. Although many successful  
106 systems have been designed and developed, based on human engineered features,

107 for various tasks in computational histopathology, the generality/applicability of  
108 such systems to different tasks or to different cohorts can sometimes be limited,  
109 as a result, systems based on unsupervised feature learning have been built with  
110 demonstrated advantages especially for the study of large cohorts, among which,  
111 both the authors in [Huang et al. \(2011\)](#) and [Chang et al. \(2013c\)](#) utilized sparse  
112 coding techniques for unsupervised characterization of tissue morphometric pat-  
113 terns.

114 Furthermore, tissue histology classification can be considered as a specific  
115 application of image categorization in the context of computer vision research,  
116 where spatial pyramid matching (SPM) [Lazebnik et al. \(2006\)](#) has clearly be-  
117 come the major component of the state-of-art systems [Everingham et al. \(2012\)](#)  
118 for its effectiveness in practice. Meanwhile, sparsity/locality-constrained feature  
119 encoders, through dictionary learning, have also been widely studied, and the im-  
120 provement in classification performance has been confirmed in various applica-  
121 tions [Yang et al. \(2009\)](#); [Wang et al. \(2010\)](#); [Chang et al. \(2013a\)](#).

122 The evolution of our research on the classification of histology sections con-  
123 tains several stages: (i) kernel-based classification built-upon human engineered  
124 feature (e.g., SIFT features) [Han et al. \(2011\)](#); (ii) independent subspace analy-  
125 sis for unsupervised discovery of morphometric signatures without the constraint  
126 of being able to reconstruct the original signal [Le et al. \(2012\)](#); (iii) single layer  
127 predictive sparse decomposition for unsupervised discovery of morphometric sig-  
128 natures with the constraint of being able to reconstruct the original signal [Nayak  
129 et al. \(2013\)](#); (iv) combination of either prior knowledge [Chang et al. \(2013a\)](#) or  
130 predictive sparse decomposition [Chang et al. \(2013c\)](#) with spatial pyramid match-  
131 ing; and (v) more recently, stacking multiple predictive sparse coding modules  
132 into deep hierarchy [Chang et al. \(2013d\)](#). And this paper builds on our longstand-  
133 ing expertise and experiences to provide (i) extensive evaluation on the model  
134 architecture for the classification of histology sections; and (ii) insights on several  
135 fundamental questions for the classification of histology sections, which, hope-  
136 fully, will shed lights on the analysis of histology sections in large cohorts towards  
137 the ultimate goal of improved therapy and treatment.

### 138 **3. Model Architecture**

139 To ensure the extensive evaluation and detailed insights on impact of the  
140 key components during the architecture construction, we have systematically ex-  
141 perimented the model architecture with various combinations of feature types,  
142 feature extraction strategies and intermediate layers based on sparsity/locality-

Table 1: Annotation of abbreviations in the paper, where FE stands for feature extraction; SFE stands for sparse feature encoding; and SPM stands for spatial pyramid matching. Here, we also provide the dimension information about (i) original features (outcome of FE); (ii) sparse codes (outcome of SFE); (iii) final representation (outcome of final spatial pooling, i.e., SPM); and (iv) final prediction (outcome of architectures as a one-dimensional class label.)

Category	Abbreviation	Description	Dimension
FE	CMF	Cellular Morphometric Feature	15
	DSIFT	Dense SIFT	128
	SSIFT	Salient SIFT	128
	DCT	Dense [Color,Texture]	203
	SCT	Salient [Color,Texture]	203
	DPSD	Dense PSD	1024
	SPSD	Salient PSD	1024
SFE	SC	Sparse Coding	1024
	GSC	Graph Regularized Sparse Coding	1024
	LLC	Locality-Constraint Linear Coding	1024
	LCDL	Locality-Constraint Dictionary Learning	1024
SPM	KSPM	Kernal SPM	(256, 512, 1024)
	LSPM	Linear SPM	(256, 512, 1024)
Architecture	FE-KSPM	Architectures without the sparse feature encoder	1
	FE-SFE-LSPM	Architectures with the sparse feature encoder	1

143 constrained feature encoders. And this section describes how we built the tissue  
 144 classification architecture for evaluation. Table 1 and Table 2 summarize the aber-  
 145 rations and important terms, respectively, and detailed descriptions are listed in  
 146 the sections as follows,

### 147 3.1. Feature Extraction Modules (FE)

148 The major barrier in tissue histology classification, in large cohorts, stems  
 149 from the large technical variations and biological heterogeneities, which requires  
 150 the feature representation to capture the intrinsic properties in the data. In this  
 151 work, we have evaluated three different features from two different categories  
 152 (i.e., human-engineered feature and unsupervised feature learning). Details are as  
 153 follows,

154 **Cellular Morphometric Feature - CMF:** The cellular morphometric features  
 155 are human-engineered biological meaningful cellular-level features, which are ex-  
 156 tracted based on segmented nuclear regions over the input image. It has been re-  
 157 cently shown that tissue classification systems based on CMF are insensitive to

Table 2: Annotation of important terms used in this paper.

Term	Description
Human Engineered Features	Refers to features that are pre-determined by human experts, with manually fixed filters/kernels/templates during extraction.
Cellular Prior Knowledge	Refers to the morphometric information, in terms of shape, intensity, etc., that are extracted from each individual cell/nucleus
Cellular Saliency	Refers to perceptually salient regions corresponding to cells/nuclei in tissue histology sections.
Multi-Stage System	Specifically refers to the architectures with multiple stacked feature extraction/abstraction layers.
Single-Stage System	Specifically refers to the architectures with a single feature extraction layer.

158 segmentation strategies [Chang et al. \(2013a\)](#). In this work, we employ the seg-  
 159 mentation strategy proposed in [Chang et al. \(2013b\)](#), and simply use the same set  
 160 of features as described in Table 3. It is worth to mention that although generic cel-  
 161 lular features, e.g., Zernike moments [Apostolopoulos et al. \(2011\)](#); [Asadi et al.](#)  
 162 [\(2006\)](#), have been successfully applied in various biomedical applications, we  
 163 choose to use CMF due to (i) its demonstrated power in tissue histology classifi-  
 164 cation [Chang et al. \(2013a\)](#); and (ii) the limited impact by including those generic  
 165 cellular features on both evaluation and understanding of the benefits introduced  
 166 by the sparse feature encoders.

167 **Dense SIFT - DSIFT:** The dense SIFT features are human-engineered fea-  
 168 tures, which are extracted from regularly-spaced patches over the input image,  
 169 with the fixed patch-size ( $16 \times 16$  pixels) and step-size (8 pixels).

170 **Salient SIFT - SSIFT:** The salient SIFT features are human-engineered fea-  
 171 tures, which are extracted from patches centered at segmented nuclear centers [Chang](#)  
 172 [et al. \(2013b\)](#) over the input image, with a fixed patch-size ( $16 \times 16$  pixels).

173 **Dense [Color,Texture] - DCT:** The dense [Color,Texture] features are human  
 174 engineered features, and formed as a concatenation of texture and mean color  
 175 with the fixed patch-size ( $20 \times 20$  pixels) and step-size (20 pixels), where color  
 176 features are extracted in the RGB color space, and texture features (in terms of  
 177 mean and variation of filter responses) are extracted via steerable filters [Young](#)  
 178 [and Lesperance \(2001\)](#) with 8 directions ( $\theta \in \{0, \frac{\pi}{8}, \frac{\pi}{4}, \frac{3\pi}{8}, \frac{1\pi}{2}, \frac{5\pi}{8}, \frac{3\pi}{4}, \frac{7\pi}{8}\}$ ) and 5  
 179 scales ( $\sigma \in \{1, 2, 3, 4, 5\}$ ) on the grayscale image.

180 **Salient [Color,Texture] - SCT:** The salient [Color,Texture] features are human-  
 181 engineered features, which are extracted on patches centered at segmented nuclear  
 182 centers [Chang et al. \(2013b\)](#) over the input image, with a fixed patch-size ( $20 \times 20$



Table 3: Cellular morphometric features, where the curvature values were computed with  $\sigma = 2.0$ , and the nuclear background region is defined to be the region outside the nuclear region, but inside the bounding box of nuclear boundary.

Feature	Description
Nuclear Size	#pixels of a segmented nucleus
Nuclear Voronoi Size	#pixels of the voronoi region, where the segmented nucleus resides
Aspect Ratio	Aspect ratio of the segmented nucleus
Major Axis	Length of Major axis of the segmented nucleus
Minor Axis	Length of Minor axis of the segmented nucleus
Rotation	Angle between major axis and x axis of the segmented nucleus
Bending Energy	Mean squared curvature values along nuclear contour
STD Curvature	Standard deviation of absolute curvature values along nuclear contour
Abs Max Curvature	Maximum absolute curvature values along nuclear contour
Mean Nuclear Intensity	Mean intensity in nuclear region measured in gray scale
STD Nuclear Intensity	Standard deviation of intensity in nuclear region measured in gray scale
Mean Background Intensity	Mean intensity of nuclear background measured in gray scale
STD Background Intensity	Standard deviation of intensity of nuclear background measured in gray scale
Mean Nuclear Gradient	Mean gradient within nuclear region measured in gray scale
STD Nuclear Gradient	Standard deviation of gradient within nuclear region measured in gray scale

183 pixels).

184 **Dense PSD - DPSD:** The unsupervised features are learned by predictive  
185 sparse decomposition (PSD) on randomly sampled image patches following the  
186 protocol in [Chang et al. \(2013c\)](#), and the dense PSD features are extracted from  
187 regularly-spaced patches over the input image, with the fixed patch-size ( $20 \times 20$   
188 pixels), step-size (20 pixels) and number of basis functions (1024). Briefly, given  
189  $\mathbf{X} = [\mathbf{x}_1, \dots, \mathbf{x}_N] \in \mathbb{R}^{m \times N}$  as a set of vectorized image patches, we formulated  
190 the PSD optimization problem as:

$$\begin{aligned}
 \min_{\mathbf{B}, \mathbf{Z}, \mathbf{W}} \quad & \|\mathbf{X} - \mathbf{BZ}\|_F^2 + \lambda \|\mathbf{Z}\|_1 + \|\mathbf{Z} - \mathbf{WX}\|_F^2 \\
 \text{s.t.} \quad & \|\mathbf{b}_i\|_2^2 = 1, \forall i = 1, \dots, h
 \end{aligned} \tag{1}$$

191 where  $\mathbf{B} = [\mathbf{b}_1, \dots, \mathbf{b}_h] \in \mathbb{R}^{m \times h}$  is a set of the basis functions;  $\mathbf{Z} = [\mathbf{z}_1, \dots, \mathbf{z}_N] \in$   
192  $\mathbb{R}^{h \times N}$  is the sparse feature matrix;  $\mathbf{W} \in \mathbb{R}^{h \times m}$  is the auto-encoder;  $\lambda$  is the  
193 regularization constant. The goal of jointly minimizing Eq. (1) with respect to the  
194 triple  $\langle \mathbf{B}, \mathbf{Z}, \mathbf{W} \rangle$  is to enforce the inference of the regressor  $\mathbf{WX}$  to be resemble  
195 to the optimal sparse codes  $\mathbf{Z}$  that can reconstruct  $\mathbf{X}$  over  $\mathbf{B}$  [Kavukcuoglu et al.](#)  
196 (2008). In our implementation, the number of basis functions ( $\mathbf{B}$ ) is fixed to be  
197 1024,  $\lambda$  was fixed to be 0.3, empirically, for the best performance.

198 **Salient PSD - SPSD:** The salient PSD features are extracted on patches centered  
199 at segmented nuclear centers [Chang et al. \(2013b\)](#) over the input image, with

Table 4: Properties of various features in evaluation. Note, all human-engineered features are pre-determined and dataset independent; while features from unsupervised feature learning are task/dataset-dependent, and are able to capture task/dataset-specific information, such as potentially meaningful morphometric patterns in tissue histology.

FE	Design	Target	Biological Information
CMF	Human-Engineered	Cell (dataset independent)	Cellular morphometric information
SIFT	Human-Engineered	Generic (dataset independent)	NA
CT	Human-Engineered	Color and texture patterns (dataset independent)	NA
PSD	Learned	Generic (dataset dependent)	Dataset dependent

200 the fixed patch-size ( $20 \times 20$  pixels) and fixed number of basis functions (1024).

201 The properties of aforementioned features are summarized in Table 4. Note  
 202 that salient features are not included, given the fact that they only differ from their  
 203 corresponding dense versions with extra saliency information. It is clear that,  
 204 different from SIFT and CT, which are generic features designed for general pur-  
 205 poses, both CMF and PSD can encode biological meaningful information, where  
 206 the former works in a pre-determined manner while the latter has the potential  
 207 to capture biological meaningful patterns in an unsupervised fashion. Therefore,  
 208 within the context of tissue histology classification, CMF and PSD have the po-  
 209 tential to work better due to these intrinsic properties, as shown in our evaluation.

### 210 3.2. Sparse Feature Encoding Modules (SFE)

211 It has been shown recently [Yang et al. \(2009\)](#); [Wang et al. \(2010\)](#) that the  
 212 impose of the feature encoder through dictionary learning, with sparsity or local-  
 213 ity constraint, significantly improves the efficacy of existing image classification  
 214 systems. *The rationale is that the sparse feature encoder functions as an ad-*  
 215 *ditional feature extraction/abstraction operation, and thus adds an extra layer*  
 216 *(stage) to the feature extraction component of the system. Therefore, it extends*  
 217 *the original system with multiple feature extraction/abstraction stages, which is*  
 218 *able to capture intrinsic patterns at the higher-level, as suggested in [Jarrett et al.](#)*  
 219 *(2009).* To study the impact of the sparse feature encoder on tissue histology  
 220 classification, we adopt three different sparsity/locality-constrained feature en-  
 221 coders for evaluation. Briefly, let  $\mathbf{Y} = [\mathbf{y}_1, \dots, \mathbf{y}_M] \in \mathbb{R}^{a \times M}$  be a set of features,  
 222  $\mathbf{C} = [\mathbf{c}_1, \dots, \mathbf{c}_M] \in \mathbb{R}^{b \times M}$  be the set of sparse codes, and  $\mathbf{B} = [\mathbf{b}_1, \dots, \mathbf{b}_b] \in \mathbb{R}^{a \times b}$   
 223 be a set of basis functions for feature encoding, the feature encoders are summa-  
 224 rized as follows,

225 **Sparse Coding - (SC):**

$$\min_{\mathbf{B}, \mathbf{C}} \sum_{i=1}^M \|\mathbf{y}_i - \mathbf{B}\mathbf{c}_i\|^2 + \lambda \|\mathbf{c}_i\|_1; \quad \text{s.t. } \|\mathbf{b}_i\| \leq 1, \forall i \quad (2)$$

226 where  $\|\mathbf{b}_i\|$  is a unit  $\ell_2$ -norm constraint for avoiding trivial solutions, and  $\|\mathbf{c}_i\|_1$   
 227 is the  $\ell_1$ -norm enforcing the sparsity of  $\mathbf{c}_i$ . In our implementation, the number of  
 228 basis functions ( $\mathbf{B}$ ) is fixed to be 1024,  $\lambda$  is fixed to be 0.15, empirically, for the  
 229 best performance.

230 **Graph Regularized Sparse Coding - (GSC) Zheng et al. (2011)**

$$\min_{\mathbf{B}, \mathbf{C}} \sum_{i=1}^M \|\mathbf{y}_i - \mathbf{B}\mathbf{c}_i\|^2 + \lambda \|\mathbf{c}_i\|_1 + \alpha \text{Tr}(\mathbf{C}\mathbf{L}\mathbf{C}^T); \quad \text{s.t. } \|\mathbf{b}_i\| \leq 1, \forall i \quad (3)$$

231 where  $\|\mathbf{b}_i\|$  is a unit  $\ell_2$ -norm constraint for avoiding trivial solutions, and  $\|\mathbf{c}_i\|_1$   
 232 is the  $\ell_1$ -norm enforcing the sparsity of  $\mathbf{c}_i$ ,  $\text{Tr}(\cdot)$  is the trace of matrix  $\cdot$ ,  $\mathbf{L}$  is the  
 233 Laplacian matrix, and the third term encodes the Laplacian regularizer Belkin and  
 234 Niyogi (2003). Please refer to Zheng et al. (2011) for details of the formulation.  
 235 In our implementation, the number of basis functions ( $\mathbf{B}$ ) is fixed to be 1024, the  
 236 regularization parameters,  $\lambda$  and  $\alpha$  are fixed to be 1 and 5, respectively, for the  
 237 best performance.

238 **Locality-Constraint Linear Coding - (LLC) Wang et al. (2010):**

$$\min_{\mathbf{B}, \mathbf{C}} \sum_{i=1}^M \|\mathbf{y}_i - \mathbf{B}\mathbf{c}_i\|^2 + \lambda \|\mathbf{d}_i \odot \mathbf{c}_i\|_1; \quad \text{s.t. } \mathbf{1}^\top \mathbf{c}_i = 1, \forall i \quad (4)$$

239 where  $\odot$  denotes the element-wise multiplication, and  $\mathbf{d}_i \in \mathbb{R}^b$  encodes the simi-  
 240 larity of each basis vector to the input descriptor  $\mathbf{y}_i$ , Specifically,

$$\mathbf{d}_i = \exp\left(\frac{\text{dist}(\mathbf{y}_i, \mathbf{B})}{\sigma}\right) \quad (5)$$

241 where  $\text{dist}(\mathbf{y}_i, \mathbf{B}) = [\text{dist}(\mathbf{y}_i, \mathbf{b}_1), \dots, \text{dist}(\mathbf{y}_i, \mathbf{b}_b)]$ ,  $\text{dist}(\mathbf{y}_i, \mathbf{b}_j)$  is the Euclidean  
 242 distance between  $\mathbf{y}_i$  and  $\mathbf{b}_j$ ,  $\sigma$  is used to control the weight decay speed for the  
 243 locality adaptor. In our implementation, the number of basis functions ( $\mathbf{B}$ ) is  
 244 fixed to be 1024, the regularization parameters  $\lambda$  and  $\sigma$  are fixed to be 500 and  
 245 100, respectively, to achieve the best performance.

246 **Locality-Constraint Dictionary Learning - (LCDL) Zhou and Barner (2013):**

247 The LCDL optimization problem is formulated as:

$$\begin{aligned}
& \min_{\mathbf{B}, \mathbf{C}} \|\mathbf{Y} - \mathbf{BC}\|_F^2 + \lambda \sum_{i=1}^N \sum_{j=1}^K \left[ c_{ji}^2 \|\mathbf{y}_i - \mathbf{b}_j\|_2^2 \right] + \mu \|\mathbf{C}\|_F^2 & (6) \\
& \text{s.t.} \quad \begin{cases} \mathbf{1}^T \mathbf{c}_i = 1 & \forall i & (*) \\ c_{ji} = 0 & \text{if } \mathbf{b}_j \notin \Omega_\tau(\mathbf{y}_i) & \forall i, j & (**) \end{cases}
\end{aligned}$$

248 where  $\Omega_\tau(\mathbf{y}_i)$  is defined as the  $\tau$ -neighborhood containing  $\tau$  nearest neighbors of  
249  $\mathbf{y}_i$ , and  $\lambda, \mu$  are positive regularization constants.  $\mu \|\mathbf{C}\|_F^2$  is included for numerical  
250 stability of the least-squares solution. The sum-to-one constraint (\*) follows  
251 from the symmetry requirement, while the locality constraint (\*\*) ensures that  $\mathbf{y}_i$   
252 is reconstructed by atoms belonging to its  $\tau$ -neighborhood, allowing  $\mathbf{c}_i$  to char-  
253 acterize the intrinsic local geometry. In our implementation, the number of basis  
254 functions ( $\mathbf{B}$ ) is fixed to be 1024, the regularization parameters  $\lambda$  and  $\mu$  are fixed  
255 to be 0.3 and 0.001, respectively, and the neighborhood size  $\tau$  is fixed to be 5,  
256 empirically, to achieve the best performance.

257 The major differences of aforementioned sparse feature encoders reside in two  
258 folds:

- 259 1. Objective:
  - 260 (a) SC: Learning sets of over-complete bases for efficient data represen-  
261 tation, originally applied to modeling the human visual cortex;
  - 262 (b) GSC : learning the sparse representations that explicitly take into ac-  
263 count the local manifold structure of the data;
  - 264 (c) LLC: generating descriptors for image classification by using efficient  
265 locality-enforcing term;
  - 266 (d) LCDL learning a set of landmark points to preserve the local geometry  
267 of the nonlinear manifold;
- 268 2. Locality Enforcing Strategy:
  - 269 (a) SC: None;
  - 270 (b) GSC: using graph Laplacian to enforce the smoothness of sparse rep-  
271 resentations along the geodesics of the data manifold;
  - 272 (c) LLC: using a locality adaptor which penalizes far-way samples with  
273 larger weights. During optimization, the basis functions are normal-  
274 ized after each iteration, which could cause the learned basis func-  
275 tions deviate from the original manifold and therefore lose locality-  
276 preservation property;

277 (d) LCDL deriving an upper-bound for reconstructing an intrinsic nonlin-  
278 ear manifold without imposing any constraint of the energy of basis  
279 functions;

280 It is clear that SC is the most general approach for data representation purpose. Al-  
281 though various locality-constrained sparse coding techniques have demonstrated  
282 success in many applications [Zheng et al. \(2011\)](#); [Wang et al. \(2010\)](#); [Zhou and](#)  
283 [Barner \(2013\)](#), their distance metric in Euclidean Space has imposed implicit hy-  
284 pothesis on the manifold of the target feature space, which might potentially im-  
285 pair the performance, as reflected in our evaluation.

### 286 3.3. Spatial Pyramid Matching Modules (SPM)

287 As an extension of the traditional Bag of Features (BoF) model, SPM has  
288 become a major component of state-of-art systems for image classification and  
289 object recognition [Everingham et al. \(2012\)](#). Specifically, SPM consists of two  
290 steps: (i) vector quantization for the construction of dictionary from input; and  
291 (ii) histogram (i.e., histogram of dictionary elements derived in previous step)  
292 concatenation from image subregions for spatial pooling. Most recently, the ef-  
293 fectiveness of SPM for the task of tissue histology classification has also been  
294 demonstrated in [Chang et al. \(2013a,c\)](#). Therefore, we include two variations of  
295 SPM as a component of the architecture for tissue histology classification, which  
296 are described as follows,

297 **Kernel SPM (KSPM [Lazebnik et al. \(2006\)](#)):** The nonlinear kernel SPM  
298 that uses spatial-pyramid histograms of features. In our implementation, we fix  
299 the level of pyramid to be 3.

300 **Linear SPM (LSPM [Yang et al. \(2009\)](#)):** The linear SPM that uses the linear  
301 kernel on spatial-pyramid pooling of sparse codes. In our implementation, we fix  
302 the level of pyramid to be 3, and choose the max pooling function on the absolute  
303 sparse codes, as suggested in [Yang et al. \(2009\)](#); [Chang et al. \(2013a\)](#).

304 The choice of spatial pyramid matching module is made to optimize the per-  
305 formance/efficiency of the entire classification architecture. Experimentally, we  
306 find that (i) **FE-KSPM** outperforms **FE-LSPM**; and (ii) **FE-SFE-LSPM** and **FE-**  
307 **SFE-KSPM** have similar performance, while the former is more computationally  
308 efficient than the latter. Therefore, we adopt **FE-SFE-LSPM** and **FE-KSPM** dur-  
309 ing the evaluation.

310 As suggested in [Jarrett et al. \(2009\)](#), the vector quantization component of  
311 SPM can be seen as an extreme case of sparse coding, and the local histogram con-  
312 struction/concatenation component of SPM can be considered as a special form

313 of spatial pooling. As a result, SPM is conceptually similar to the combination  
314 of sparse coding with spatial pooling, and therefore is able to serve as an extra  
315 layer (stage) for feature extraction. Consequently, **FE-KSPM** can be considered  
316 as a single-stage system, and **FE-SFE-LSPM** can be considered as a multi-stage  
317 system with two feature extraction/abstraction layers.

### 318 *3.4. Classification*

319 For architecture: **FE-SFE-LSPM**, we employed the linear SVM for classifi-  
320 cation, the same as in Wang et al. (2010); Yang et al. (2009). For architecture:  
321 **FE-KSPM**, the homogeneous kernel map Vedaldi and Zisserman (2012) was first  
322 applied, followed by linear SVM for classification.

## 323 **4. Experimental Evaluation of Model Architecture**

### 324 *4.1. Experimental Setup*

325 Our extensive evaluation is performed based on the cross-validation strategy  
326 with 10 iterations, where both training and testing images are randomly selected  
327 per iteration, and the final results are reported as the mean and standard error of  
328 the correct classification rates with various dictionary sizes (256,512,1024) on the  
329 following two distinct datasets, curated from (i) Glioblastoma Multiforme (GBM)  
330 and (ii) Kidney Renal Clear Cell Carcinoma (KIRC) from The Cancer Genome  
331 Atlas (TCGA), which are publicly available from the NIH (National Institute of  
332 Health) repository. The curation is performed by our pathologist in order to pro-  
333 vide examples of distinct regions of microanatomy (e.g., stromal) and histopathol-  
334 ogy (e.g., tumor, necrosis) with sufficient amount of biological heterogeneities and  
335 technical variations, so that the classification model architecture can be faithfully  
336 tested and validated against important studies. Furthermore, the combination of  
337 extensive cross-validation and independent validation on datasets with distinct tu-  
338 mor types, to the maximum extent, ensures the consistency and unbiasedness of  
339 our findings. The detailed description of our datasets as well as the corresponding  
340 task formulation are described as follows,

341 **GBM Dataset:** In brain tumors, necrosis, proliferation of vasculature, and  
342 infiltration of lymphocytes are important prognostic factors. And, some of these  
343 analyses, such as the quantification of necrosis, have to be defined and performed  
344 as classification tasks in histology sections. Furthermore, necrosis is a dynamic  
345 process and different stages of necrosis exist (e.g., from cells initiating a necrosis  
346 process to complete loss of chromatin content). Therefore, the capability of iden-  
347 tification/classification of these end points, e.g., necrosis-related regions, in brain

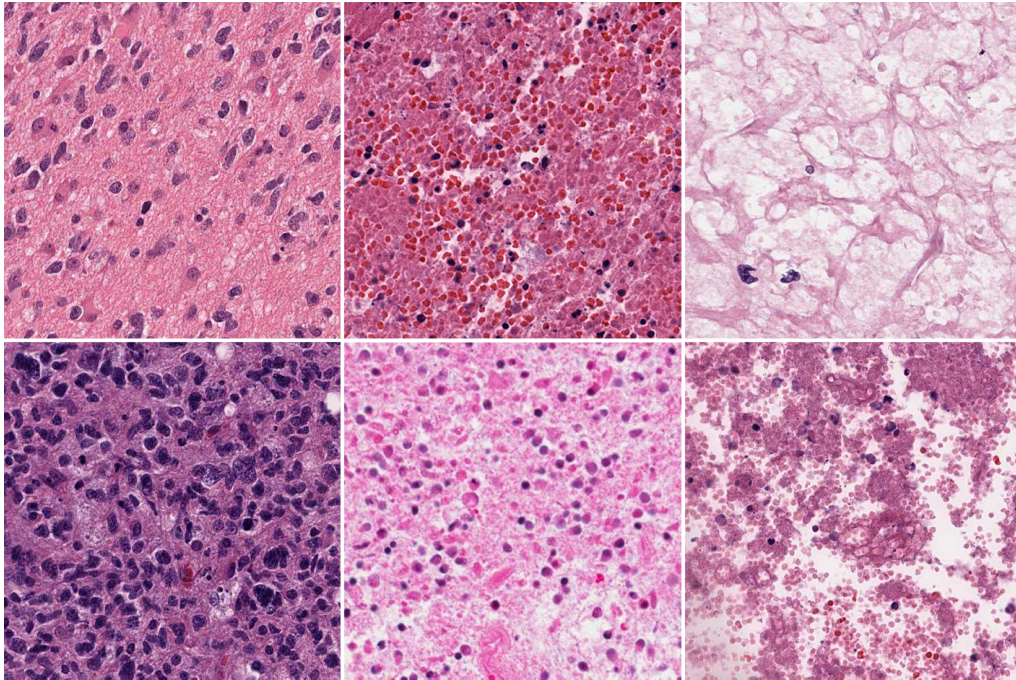


Figure 1: GBM Examples. First column: Tumor; Second column: Transition to necrosis; Third column: Necrosis. Note that the phenotypic heterogeneity is highly diverse in each column.

348 tumor histology sections, is highly demanded. In this study, we aim to validate the  
 349 model architecture for the three-category classification (i.e., Tumor, Necrosis, and  
 350 Transition to Necrosis) on the GBM dataset, where the images are curated from  
 351 the whole slide images (WSI) scanned with a 20X objective (0.502 micron/pixel).  
 352 Representative examples of each class can be found in Figure 1, which reveal  
 353 a significant amount of intra-class phenotypic heterogeneity. Such a highly het-  
 354 erogenous dataset provides an ideal test case for the quantitative evaluation of the  
 355 composition of model architecture and its impact, in terms of performance and  
 356 robustness, on the classification of histology sections. Specifically, the number  
 357 of images per category are 628, 428 and 324, respectively, and most images are  
 358  $1000 \times 1000$  pixels. For this task, we train, with various model architectures,  
 359 on 160 images per category and tested on the rest, with three different dictionary  
 360 sizes: 256, 512 and 1024.

361 **KIRC Dataset:** Recent studies on quantitative histology analysis [Lan et al.](#)  
 362 [\(2015\)](#); [Rogojanu et al. \(2015\)](#); [Huijbers et al. \(2013\)](#); [de Kruijf et al. \(2011\)](#) re-  
 363 veal that the tumor-stroma ratio is a prognostic factor in many different tumor

364 types, and it is therefore interesting and desirable to know how such an index  
365 plays its role in KIRC, which can be fulfilled with two steps as follows, (i) iden-  
366 tification/classification of tumor/stromal regions in tissue histology sections for  
367 the construction of tumor-stroma ratio; and (ii) correlative analysis of the derived  
368 tumor-stroma ratio with clinical outcome. Therefore, in this study, we aim to  
369 validate the model architecture for the three-category classification (i.e., Tumor,  
370 Normal, and Stromal) on the KIRC dataset, where the images are curated from  
371 the whole slide images (WSI) scanned with a 40X objective (0.252 micron/pixel).  
372 Representative examples of each class can be found in Figure 2, which (i) contain  
373 two different types of tumor corresponding to clear cell carcinoma, with the loss  
374 of cytoplasm (first row), and granular tumor (second row), respectively; and (ii)  
375 reveal large technical variations (i.e., in terms of staining protocol), especially in  
376 the normal category. The combination of the large amount of biological hetero-  
377 geneity and technical variations in this curated dataset provides an ideal test case  
378 for the quantitative evaluation of the composition of model architecture and its  
379 impact, in terms of performance and robustness, on the classification of histology  
380 sections. Specifically, the number of images per category are 568, 796 and 784,  
381 respectively, and most images are  $1000 \times 1000$  pixels. For this task, we train, with  
382 various model architectures, on 280 images per category and tested on the rest,  
383 with three different dictionary sizes: 256, 512 and 1024.

#### 384 4.2. *Is unsupervised feature learning preferable to human engineered features?*

385 Feature extraction is the very first step for the construction of classification/recognition  
386 system, and is one of the most important factors that affect the performance. To  
387 answer this question, we evaluated four well-selected features based on two vastly  
388 different tumor types as described previously. The evaluation was carried out with  
389 the **FE-KSPM** architecture for its simplicity, and the performance was illustrated  
390 in Figure 3 for the GBM and KIRC datasets. It is clear that the systems based on  
391 CMF (CMF-KSPM) and PSD (PSD-KSPM) have the top performances, which are  
392 due to i) the critical role of cellular morphometric context during the pathological  
393 diagnosis, as suggested in [Chang et al. \(2013a\)](#); and ii) the capability of unsuper-  
394 vised feature learning in capturing intrinsic morphometric patterns in histology  
395 sections.

#### 396 4.3. *Does Cellular Saliency Help?*

397 CMF differs from DSIFT, DCT and DPSD in that (1) CMF characterizes bi-  
398 ological meaningful properties at cellular-level, while DSIFT, DCT and DPSD  
399 are purely pixel/patch-level features without any specific biological meaning; (2)



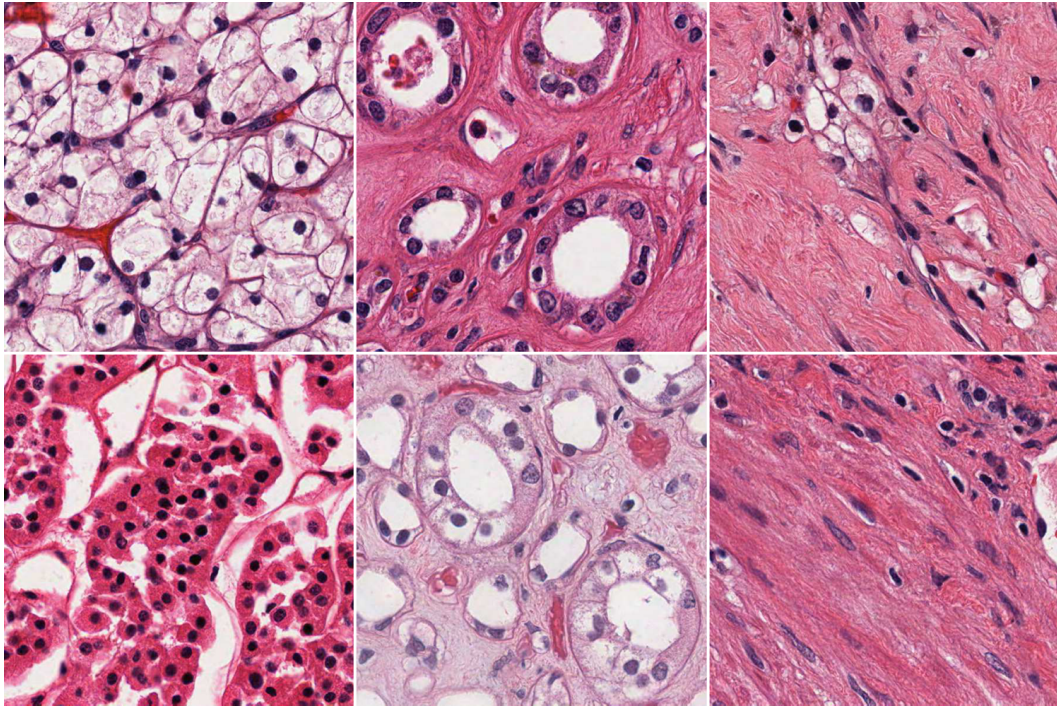


Figure 2: KIRC examples. First column: Tumor; Second column: Normal; Third column: Stromal. Note that (a) in the first column, there are two different types of tumor corresponding to clear cell carcinoma, with the loss of cytoplasm (first row), and granular tumor (second row), respectively; and (b) in the second column, staining protocol is highly varied. The cohort contains a significant amount of tumor heterogeneity that is coupled with technical variation.

400 CMF is extracted per nuclear region which is cellular-saliency-aware, while DSIFT,  
 401 DCT and DPSD are extracted per regularly-spaced image patch without using  
 402 cellular information as prior. An illustration of aforementioned feature extrac-  
 403 tion strategies can be found in Figure 4. Recent study [Wu et al. \(2013\)](#) indicates  
 404 that saliency-awareness may be helpful for the task of image classification, thus it  
 405 will be interesting to figure out whether SIFT, [Color,Texture] and PSD features  
 406 can be improved by the incorporation of cellular-saliency as prior. Therefore,  
 407 we design salient SIFT (SSFIT), salient [Color,Texture] and salient PSD (SPSD)  
 408 features, which are only extracted at nuclear centroid locations. Comparison of  
 409 classification performance between dense features and salient features, with the  
 410 **FE-KSPM** architecture, is illustrated in Figure 5 for GBM and KIRC datasets,  
 411 which show that, for SIFT, [Color,Texture] and PSD features, cellular-saliency-  
 412 awareness plays a negative role for the task of tissue histology classification. One

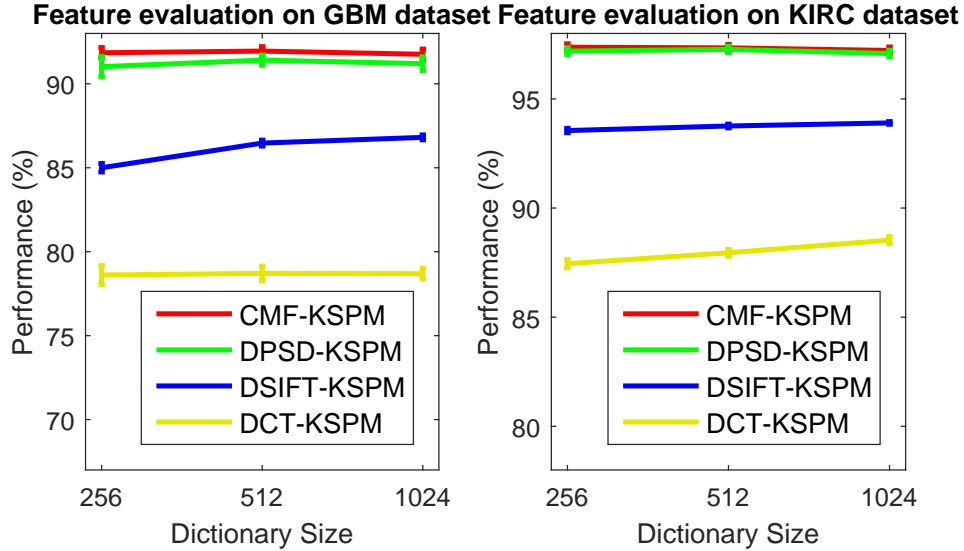


Figure 3: Evaluation of different features with **FE-KSPM** architecture on both GBM (left) and KIRC (right) datasets. Here, the performance is reported as the mean and standard error of the correct classification rate, as detailed in Section 4.

413 possible explanation is that, different from CMF, which encodes specific biological  
 414 meanings and summarizes tissue image with intrinsic biological-context-based  
 415 representation, SIFT, [Color,Texture] and PSD lead to appearance-based image  
 416 representation, and thus require dense sampling all over the place in order to faith-  
 417 fully assemble the view of the image.

#### 418 4.4. Does the Sparse Feature Encoder Help?

419 The evaluation of systems with the sparse feature encoder is carried out with  
 420 the configuration **FE-SFE-LSPM**, where LSPM is used instead of KSPM for im-  
 421 proved efficiency. Classification performance is illustrated in Figure 6 and Fig-  
 422 ure 7 for the GBM and KIRC datasets, respectively; and the results show that,  
 423 compared to **FE-KSPM**,

- 424 1. For  $\mathbf{FE}=\mathbf{CMF}$  and  $\mathbf{SFE}\in\{\mathbf{SC,GSC,LLC,LCDL}\}$ , **FE-SFE-LSPM** consis-  
 425 tently improves the classification performance for both GBM and KIRC  
 426 datasets;
- 427 2. For  $\mathbf{FE}\in\{\mathbf{SIFT,[Color,Texture]}\}$  and  $\mathbf{SFE}\in\{\mathbf{SC,GSC,LLC,LCDL}\}$ , **FE-SFE-**  
 428 **LSPM** improves the performance for KIRC dataset; while impairs the per-  
 429 formance for GBM dataset;

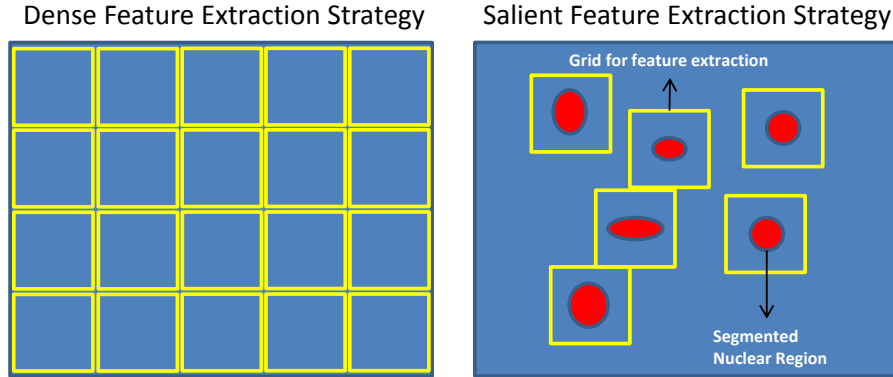


Figure 4: Illustration of dense feature extraction strategy (left) and salient feature extraction strategy (right), where dense features are extracted on regularly-spaced patches, while salient features are extracted on patches centered at segmented nuclear centers. Here, yellow rectangle and red blob represent feature extraction patch/grid and segmented nuclear region, respectively.

- 430 3. For **FE=PSD**, **FE-SFE-LSPM** improves the performance for both GBM  
 431 and KIRC datasets, with **SFE = SC**; while, in general, impairs the perfor-  
 432 mance for both datasets, with **SFE**  $\in$  {GSC, LLC, LCDL}.

433 The observations above suggest that, the effect of the sparse feature encoder  
 434 highly correlates with the robustness of the features being used, and significant im-  
 435 provement of performance can be achieved consistently across different datasets  
 436 with the choice of CMF. It is also interesting to notice that, with the choice of  
 437 PSD, the sparse feature encoder only helps improve the performance with sparse  
 438 coding (SC) as the intermediate feature extraction layer. A possible explanation  
 439 is that, compared to CMF which has real physical meanings, the PSD feature  
 440 resides in a hyper space constructed from unsupervised feature learning, where  
 441 Euclidean-distance, as a critical part of GSC, LLC and LCDL, may not apply.

442 Furthermore, it is also interesting and important to know the effect of incor-  
 443 porating deep learning for feature extraction. Therefore, for further validation,  
 444 we have also evaluated two popular deep learning techniques, namely Stacked  
 445 PSD [Chang et al. \(2013d\)](#) and Convolutional Neural Networks (CNN) [Lecun](#)  
 446 [et al. \(1998\)](#); [Huang and LeCun \(2006\)](#); [Krizhevsky et al. \(2012\)](#). Specifically,

- 447 1. StackedPSD-KSPM: for the evaluation of Stacked PSD, the same proto-  
 448 col as in [Chang et al. \(2013d\)](#) is utilized. Briefly, two layers of PSD, with  
 449 2048 (first layer) and 1024 (second layer) basis functions, respectively, are  
 450 stacked to form a deep architecture for the feature extraction on  $20 \times 20$

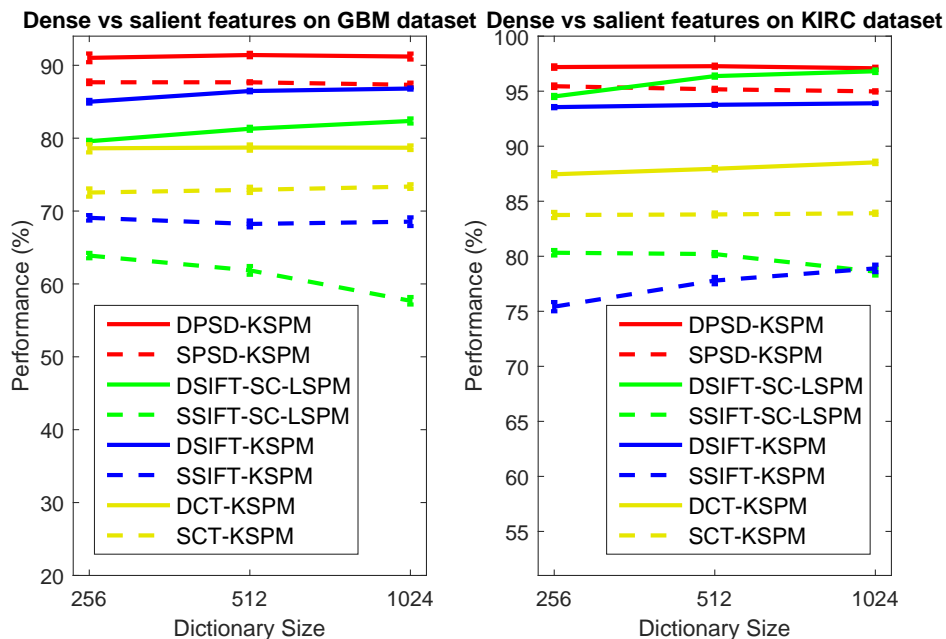


Figure 5: Evaluation of dense feature extraction and salient feature extraction strategies with the **FE-KSPM** architecture on both GBM (left) and KIRC (right) datasets, where solid line and dashed line represent systems built upon dense feature and salient feature, respectively. Here, the performance is reported as the mean and standard error of the correct classification rate, as detailed in Section 4.

- 451 image-patches with a step-size fixed to be 20, empirically, for best perfor-  
 452 mance. After the patch-based extraction, the same protocol as shown in  
 453 **FE-KSPM** is utilized for classification.
- 454 2. AlexNet-KSPM: for the evaluation of CNN, we adopt one of the most pow-  
 455 erful deep neural network architecture: AlexNet [Krizhevsky et al. \(2012\)](#)  
 456 with the Caffe [Jia et al. \(2014\)](#) implementation. Given (i) the extremely  
 457 large scale (60 million parameters) of the AlexNet architecture; (ii) the sig-  
 458 nificantly smaller data-scale of GBM and KIRC, compared to ImageNet [Deng](#)  
 459 [et al. \(2009\)](#) with one thousand categories and millions of images, where  
 460 AlexNet is originally trained; and (iii) the significant decline of performance  
 461 due to over-fitting that we experience with the end-to-end tuning of AlexNet  
 462 on our dataset as a result of (i) and (ii), we simply adopt the pre-trained  
 463 AlexNet for feature extraction on  $224 \times 224$  image-patches with a step-size  
 464 fixed to be 45, empirically, for best performance. After the patch-based

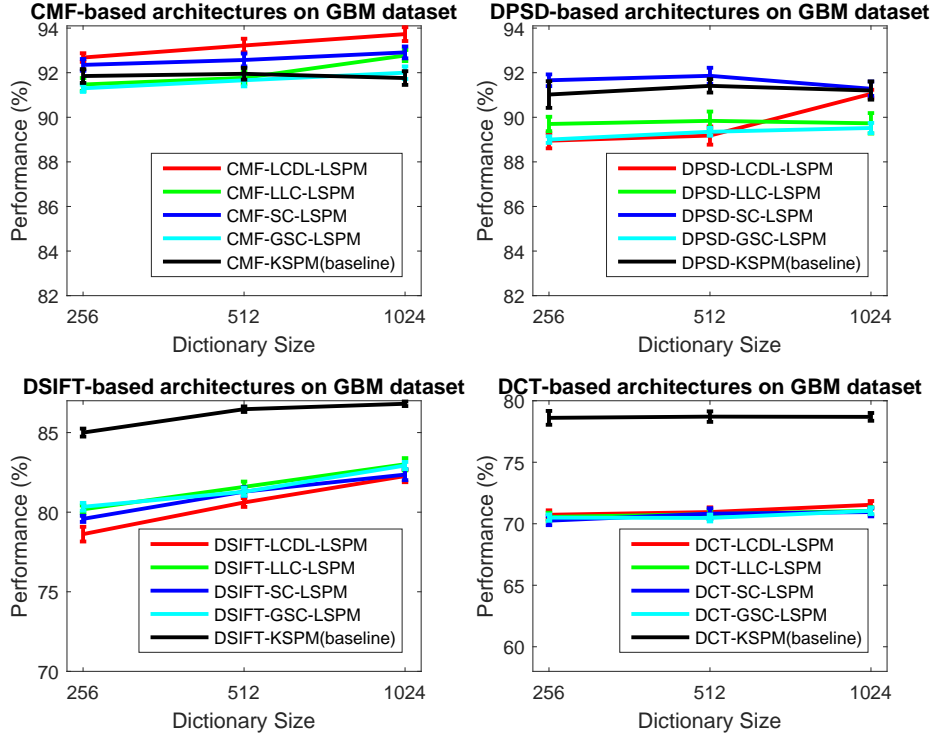


Figure 6: Evaluation of the architectures with sparse feature encoders (**FE-SFE-LSPM**) on GBM dataset. Here, the performance is reported as the mean and standard error of the correct classification rate, as detailed in Section 4.

465 extraction, the same protocol as shown in **FE-KSPM** is utilized for classifi-  
 466 cation. It is worth to mention that such an approach falls into the categories  
 467 of both deep learning and transfer learning.

468 Experimental results, illustrated in Figure 8, suggest that,

- 469 1. Both sparse feature encoders and feature extraction strategies based on deep  
 470 learning techniques consistently improve the performance of tissue histol-  
 471 ogy classification;
- 472 2. The extremely large-scale convolutional deep neural networks (e.g., AlexNet),  
 473 pre-trained on extremely large-scale dataset (e.g., ImageNet), can be di-  
 474 rectly applicable to the task of tissue histology classification due to the ca-  
 475 pability of deep neural networks in capturing transferable base knowledge  
 476 across domains [Yosinski et al. \(2014\)](#). Although the fine-tuning of AlexNet

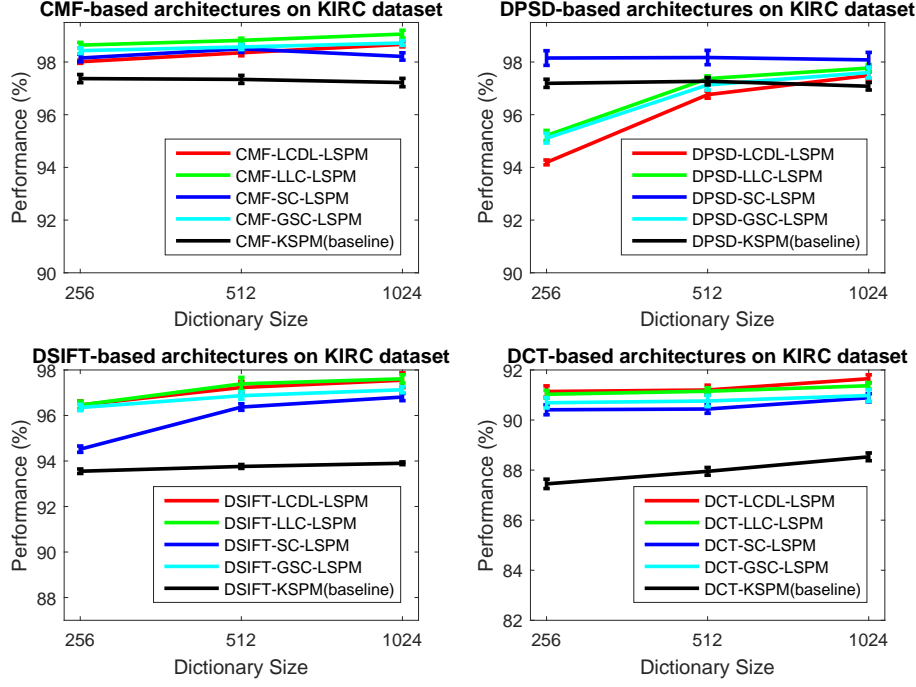


Figure 7: Evaluation of the architectures with sparse feature encoders (**FE-SFE-LSPM**) on KIRC dataset. Here, the performance is reported as the mean and standard error of the correct classification rate, as detailed in Section 4.

477 towards our datasets shows significant performance drop due to the problem  
 478 of over-fitting, the direct deployment of pre-trained deep neural networks  
 479 still provides a promising solution for tasks with limited data and labels,  
 480 which is very common in the field of medical image analysis.

481

#### 482 4.5. Revisit on Spatial Pooling

483 To further study the impact of pooling strategy, we also provide extensive  
 484 experimental evaluation on one of the most popular pooling strategies (i.e., *max*  
 485 pooling) in place of spatial pyramid matching within **FE-SFE-LSPM** framework,  
 486 which is defined as follows,

$$max : f_j = \max\{|c_{1j}|, |c_{2j}|, \dots, |c_{Mj}|\} \quad (7)$$

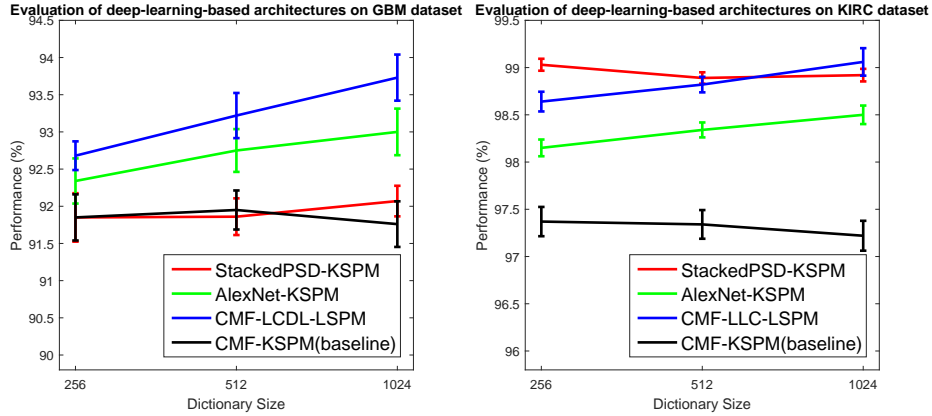


Figure 8: Evaluation of the effect of incorporating deep learning for feature extraction on both GBM and KIRC datasets. Note that, given the various combinations of **FE-SFE-LSPM**, CMF-LCDL-LSPM and CMF-LLC-LSPM are chosen for GBM and KIRC datasets, respectively, for their best performance. Here, the performance is reported as the mean and standard error of the correct classification rate, as detailed in Section 4.

487 where  $\mathbf{C} = [\mathbf{c}_1, \dots, \mathbf{c}_M] \in \mathbb{R}^{b \times M}$  is the set of sparse codes extracted from an im-  
488 age,  $c_{ij}$  is the matrix element at  $i$ -th row and  $j$ -th column of  $\mathbf{C}$ , and  $f = [f_1, \dots, f_b]$   
489 is the pooled image representation. The choice of  $\max$  pooling procedure has  
490 been justified by both biophysical evidence in the visual cortex [Serre et al. \(2005\)](#)  
491 and researches in image categorization [Yang et al. \(2009\)](#), and the derived archi-  
492 tecture is described as **FE-SFE-Max**. In our experimental evaluation, we focus on  
493 the top-two-ranked features (i.e., DPSD and CMF), where the corresponding compar-  
494 isons of classification performance are illustrated in Figure 9. It is clear that  
495 systems with SPM pooling consistently outperforms systems with  $\max$  pooling  
496 with various combinations of feature types and sparse feature encoders. A possi-  
497 ble explanation is that the vector quantization step in SPM can be considered as an  
498 extreme case of sparse coding (i.e., with a single non-zero element in each sparse  
499 code); and the local histogram concatenation step in SPM can be considered as  
500 a special form of spatial pooling. As a result, SPM is conceptually similar to an  
501 extra layer of sparse feature encoding and spatial pooling, as suggested in [Jarrett](#)  
502 [et al. \(2009\)](#), and therefore leads to an improved performance, compared to the  
503 architecture with  $\max$  pooling.

504 *4.6. Revisit on Computational Cost*

505 In addition to classification performance, another critical factor, in clinical  
506 practice, is the computational efficiency. Therefore, in this section, we provided a  
507 detailed evaluation on computational cost of various systems. Given the fact that  
508 (i) training can always be carried out off-line; (ii) the classification of the systems  
509 in evaluation are all based on linear SVM, our evaluation on computational effi-  
510 ciency focuses on on-line feature extraction (including sparse feature encoding),  
511 which is the most time-consuming part during the testing phase. As shown in  
512 Table 5,

- 513 1. SIFT features are the most computational efficient features among all the  
514 ones in comparison. However, the systems built on SIFT features greatly  
515 suffer from the technical variations and biological heterogeneities in both  
516 datasets, and therefore are not good choices for the classification of tissue  
517 histology sections;
- 518 2. Given the fact that the nuclear segmentation is a prerequisite for salient  
519 feature extraction (e.g., SPSD, SSIFT and SCT), systems built upon salient  
520 features may not be necessarily more efficient than systems built upon dense  
521 features. Furthermore, since the salient features typically impair the tissue  
522 histology classification performance, they are therefore not recommended;
- 523 3. The gain in performance of sparse feature encoders in our evaluation is at  
524 the cost of computational efficiency. And the scalability of derived systems  
525 can be improved by (i) the development of more computational-efficient  
526 algorithms, which was demonstrated in Table 6; and (ii) the deployment  
527 of advanced computational techniques, such as cluster computing or GPU  
528 acceleration for clinical deployment, which was demonstrated in Table 5 for  
529 AlexNet.
- 530 4. Most interestingly, the sparse feature encoder, based on CMF-SFE, is much  
531 more efficient even compared to many shallow architectures based on PSD  
532 or CT features; and, it is only 5% slower compared to its corresponding  
533 shallow version, based on CMF. The computational efficiency are due to (i)  
534 the high sparsity of nuclei compared to dense image patches (e.g., 350 nu-  
535 clei/image v.s. 2000 patches/image); and (ii) the extremely low dimension-  
536 ality of cellular morphometric features compared to other features (e.g., 15  
537 nuclear morphometric features v.s. 128 SIFT features, 203 CT features and  
538 1024 PSD features). Furthermore, in computational histopathology, both  
539 nuclear-level information (based on nuclear segmentation) and patch-level



540 information (based on tissue histology classification) are very critical com-  
 541 ponents, which means the nuclear segmentation results can be shared across  
 542 different tasks for the further improvement of the efficiency of multi-scale  
 543 integrated analyses.

544 To further improve the scalability of systems built-upon CMF-**SFE**, as a demon-  
 545 stration of algorithmic-scaling-up of sparse feature encoders, we constructed a  
 546 predictive sparse feature encoder (**PredictiveSFE**) in place of **SFE** as follows, to  
 547 approximate the morphometric sparse codes, specifically, provided by Equation 2,

$$\begin{aligned} \min_{\mathbf{B}, \mathbf{C}, \mathbf{G}, \mathbf{W}} \quad & \|\mathbf{Y} - \mathbf{BC}\|_F^2 + \lambda \|\mathbf{C}\|_1 + \|\mathbf{C} - \mathbf{G}\sigma(\mathbf{WY})\|_F^2 \\ \text{s.t.} \quad & \|\mathbf{b}_i\|_2^2 = 1, \forall i = 1, \dots, h \end{aligned} \quad (8)$$

548 where  $\mathbf{Y} = [\mathbf{y}_1, \dots, \mathbf{y}_N] \in \mathbb{R}^{m \times N}$  is a set of cellular morphometric descriptors;  
 549  $\mathbf{B} = [\mathbf{b}_1, \dots, \mathbf{b}_h] \in \mathbb{R}^{m \times h}$  is a set of the basis functions;  $\mathbf{C} = [\mathbf{c}_1, \dots, \mathbf{c}_N] \in$   
 550  $\mathbb{R}^{h \times N}$  is the sparse feature matrix;  $\mathbf{W} \in \mathbb{R}^{h \times m}$  is the auto-encoder;  $\sigma(\cdot)$  is the  
 551 element-wise sigmoid function;  $\mathbf{G} = \text{diag}(g_1, \dots, g_h) \in \mathbb{R}^{h \times h}$  is the scaling  
 552 matrix with  $\text{diag}$  being an operator aligning vector,  $[g_1, \dots, g_h]$ , along the diag-  
 553 onal; and  $\lambda$  is the regularization constant. Joint minimization of Eq. (8) w.r.t  
 554 the quadruple  $\langle \mathbf{B}, \mathbf{C}, \mathbf{G}, \mathbf{W} \rangle$ , enforces the inference of the nonlinear regressor  
 555  $\mathbf{G}\sigma(\mathbf{WY})$  to be similar to the optimal sparse codes,  $\mathbf{C}$ , which can reconstruct  
 556  $\mathbf{Y}$  over  $\mathbf{B}$  [Kavukcuoglu et al. \(2008\)](#). As shown in Algorithm 1, optimization  
 557 of Eq. (8) is iterative, and it terminates when either the objective function is be-  
 558 low a preset threshold or the maximum number of iterations has been reached.  
 559 In our implementation, the number of basis functions ( $\mathbf{B}$ ) was fixed to be 128,  
 560 and the SPAMS optimization toolbox [Mairal et al. \(2010\)](#) is adopted for efficient  
 561 implementation of OMP to compute the sparse code,  $\mathbf{C}$ , with sparsity prior set to  
 562 30. The end result is a highly efficient (see Table 6) and effective (see Figure 10)  
 563 system, CMF-**PredictiveSFE**-KSPM, for tissue histology classification.

## 564 5. Conclusions

565 This paper provides insights to the following three fundamental questions for  
 566 the task of tissue histology classification:

567 I. Is unsupervised feature learning preferable to human engineered features? The  
 568 answer is that, CMF and PSD work the best, compared to SIFT and [Color,Texture]  
 569 features, on two vastly different tumor types. The reasons are that (i) CMF en-  
 570 codes biological meaningful prior knowledge, which is widely adopted in the

Table 5: Average computational cost (measured in second) for feature extraction (including sparse feature encoding) on images with size  $1000 \times 1000$  pixels. The evaluation is carried out with Intel(R) Xeon(R) CPU X5365 @ 3.00GHz, and GeForce GTX 580.

Feature Extraction Component(s)	Average Computational Cost (in second)
Nuclear Segmentation	40
CMF-SFE	42 = Nuclear-Segmentation-Cost(40) + SFE-Cost(2)
DPSD-SFE	115 = DPSD-Cost(95) + SFE-Cost(20)
SPSD-SFE	70 = SPSPD-Cost(60) + SFE-Cost(10)
DSIFT-SFE	16 = DSIFT-Cost(10) + SFE-Cost(6)
SSIFT-SFE	47 = SSIFT-Cost(45) + SFE-Cost(2)
DCT-SFE	90 = DCT-Cost(80) + SFE-Cost(10)
SCT-SFE	108 = SCT-Cost(105) + SFE-Cost(3)
CMF	40 = Nuclear-Segmentation-Cost(40)
DPSD	95
SPSD	60 = Nuclear-Segmentation-Cost(40) + PSD-Cost(20)
DSIFT	10
SSIFT	45 = Nuclear-Segmentation-Cost(40)+SIFT-Cost(5)
DCT	80
SCT	105 = Nuclear-Segmentation-Cost(40) + SCT-Cost(65)
StackedPSD	100
AlexNet	1200/180 (CPU-Only/GPU-Acceleration)

Table 6: **PredictiveSFE** achieved 40X speed-up, compared to **SFE**, in sparse cellular morphometric feature extraction. The evaluation was carried out with Intel(R) Xeon(R) CPU X5365 @ 3.00GHz

Sparse Cellular Morphometric Feature Extraction	Average Computational Cost (in second)
PredictiveSFE	0.05
SFE	2

---

**Algorithm 1** Construction of the Predictive Sparse Feature Encoder (PredictiveSFE)

---

**Input:** Training set  $\mathbf{Y} = [\mathbf{y}_1, \dots, \mathbf{y}_N] \in \mathbb{R}^{m \times N}$

**Output:** Predictive Sparse Feature Encoder  $\mathbf{W} \in \mathbb{R}^{h \times m}$

- 1: **Initialize:** Randomly initialize  $\mathbf{B}$ ,  $\mathbf{W}$ , and  $\mathbf{G}$
  - 2: **repeat**
  - 3: Fixing  $\mathbf{B}$ ,  $\mathbf{W}$  and  $\mathbf{G}$ , minimize Eq. (8) w.r.t  $\mathbf{C}$ , where  $\mathbf{C}$  can be either solved as a  $\ell_1$ -minimization problem Lee et al. (2007) or equivalently solved by greedy algorithms, e.g., Orthogonal Matching Pursuit (OMP) Tropp and Gilbert (2007).
  - 4: Fixing  $\mathbf{B}$ ,  $\mathbf{W}$  and  $\mathbf{C}$ , solve for  $\mathbf{G}$ , which is a simple least-square problem with analytic solution.
  - 5: Fixing  $\mathbf{C}$  and  $\mathbf{G}$ , update  $\mathbf{B}$  and  $\mathbf{W}$ , respectively, using the stochastic gradient descent algorithm.
  - 6: **until** Convergence (maximum iterations reached or objective function  $\leq$  threshold)
- 

571 practice of pathological diagnosis; and (ii) PSD is able to capture intrinsic mor-  
572 phometric patterns in histology sections. As a result, both of them produce robust  
573 representation of the underlying properties preserved in the data.

574 II. Does cellular saliency help? The surprising answer is that cellular saliency  
575 does not help improve the performance for systems built upon pixel-/patch-level  
576 features. Experiments on both GBM and KIRC datasets confirm the performance-  
577 drop with salient feature extraction strategies, and one possible explanation is that  
578 both pixel-level and patch-level features are appearance-based representations,  
579 which require dense sampling all over the place in order to faithfully assemble  
580 the view of the image.

581 III. Does the sparse feature encoder contribute of recognition? The sparse feature  
582 encoder significantly and consistently improves the classification performance for  
583 systems built upon CMF; and meanwhile, it conditionally improves the perfor-  
584 mance for systems built upon PSD (PSD-SC-LSPM), with the choice of sparse  
585 coding (SC) as the intermediate feature extraction layer. It is believed that the con-  
586 sistency of performance highly correlates with the robustness of the feature being  
587 used, and the improvement of performance is due to the capability of the sparse  
588 feature encoder in capturing complex patterns at the higher-level. Furthermore,  
589 this paper provides a clear evidence that deep neural networks (i.e., AlexNet), pre-  
590 trained on large scale natural image datasets (i.e., ImageNet), is directly applicable

591 to the task of tissue histology classification, which is due to the capability of deep  
592 neural networks in capturing transferable base knowledge across domains [Yosin-](#)  
593 [ski et al. \(2014\)](#). Although the fine-tuning of AlexNet towards our datasets shows  
594 significant performance drop due to the problem of over-fitting, the direct deploy-  
595 ment of pre-trained deep neural networks still provides a promising solution for  
596 tasks with limited data and labels, which is very common in the field of medical  
597 image analysis.

598 Besides the insights in the aforementioned fundamental questions, this paper  
599 also shows that the superior performance of the sparse feature encoder is at the  
600 cost of computational efficiency. However, the scalability of the sparse feature  
601 encoder can be improved by (i) the development of more computational-efficient  
602 algorithms; and (ii) the deployment of advanced computational techniques, such  
603 as cluster computing or GPU acceleration. As a demonstration, this paper pro-  
604 vides an accelerated version of CMF-SFE, namely CMF-**PredictiveSFE**, which  
605 falls into the category of algorithmic-scaling-up and achieves 40X speed-up dur-  
606 ing sparse feature encoding. The end result is a highly scalable and effective  
607 system, CMF-**PredictiveSFE**-KSPM, for tissue histology classification.

608 Furthermore, all our insights are independently validated on two large cohorts,  
609 Glioblastoma Multiforme (GBM) and Kidney Clear Cell Carcinoma (KIRC), which,  
610 to the maximum extent, ensures the consistency and unbiasedness of our findings.  
611 To the best of our knowledge, this is the first attempt that systematically provides  
612 insights to the fundamental questions aforementioned in tissue histology classi-  
613 fication; and there are reasons to hope that the configuration: **FE-SFE-LSPM**  
614 ( $\text{FE} \in \{\text{CMF}, \text{PSD}\}$ ) as well as its accelerated version: **FE-PredictiveSFE-KSPM**  
615 ( $\text{FE} \in \{\text{CMF}, \text{PSD}\}$ ), can be widely applicable to different tumor types.

## 616 Acknowledgement

617 This work was supported by NIH R01 CA184476 carried out at Lawrence  
618 Berkeley National Laboratory.

## 619 References

620 Apostolopoulos, G., Tsinopoulos, S., Dermatas, E., 2011. Recognition and identi-  
621 fication of red blood cell size using zernike moments and multicolor scattering  
622 images. In: 2011 10th International Workshop on Biomedical Engineering. pp.  
623 1–4.

- 624 Asadi, M., Vahedi, A., Amindavar, H., 2006. Leukemia cell recognition with  
625 zernike moments of holographic images. In: NORSIG 2006. pp. 214–217.
- 626 Basavanhally, A., Xu, J., Madabhushu, A., Ganesan, S., 2009. Computer-aided  
627 prognosis of ER+ breast cancer histopathology and correlating survival out-  
628 come with oncotype DX assay. In: ISBI. pp. 851–854.
- 629 Belkin, M., Niyogi, P., 2003. Laplacian eigenmaps for dimensionality reduction  
630 and data representation. *Neural Computation* 15 (6), 1373–1396.
- 631 Bhagavatula, R., Fickus, M., Kelly, W., Guo, C., Ozolek, J., Castro, C., Kovacevic,  
632 J., 2010. Automatic identification and delineation of germ layer components in  
633 *h&e* stained images of teratomas derived from human and nonhuman primate  
634 embryonic stem cells. In: ISBI. pp. 1041–1044.
- 635 Chang, H., Borowsky, A., Spellman, P., Parvin, B., 2013a. Classification of tu-  
636 mor histology via morphometric context. In: Proceedings of the Conference on  
637 Computer Vision and Pattern Recognition. pp. 2203–2210.
- 638 Chang, H., Han, J., Borowsky, A., Loss, L. A., Gray, J. W., Spellman, P. T.,  
639 Parvin, B., 2013b. Invariant delineation of nuclear architecture in glioblastoma  
640 multiforme for clinical and molecular association. *IEEE Trans. Med. Imaging*  
641 32 (4), 670–682.
- 642 Chang, H., Nayak, N., Spellman, P., Parvin, B., 2013c. Characterization of tissue  
643 histopathology via predictive sparse decomposition and spatial pyramid match-  
644 ing. *Medical image computing and computed-assisted intervention–MICCAI*.
- 645 Chang, H., Zhou, Y., Spellman, P. T., Parvin, B., 2013d. Stacked predictive sparse  
646 coding for classification of distinct regions in tumor histopathology. In: Pro-  
647 ceedings of the IEEE International Conference on Computer Vision. pp. 502–  
648 507.
- 649 Dalton, L., Pinder, S., Elston, C., Ellis, I., Page, D., Dupont, W., Blamey, R., 2000.  
650 Histological gradings of breast cancer: linkage of patient outcome with level of  
651 pathologist agreements. *Modern Pathology* 13 (7), 730–735.
- 652 de Kruijf, E. M., van Nes, J. G., van de Velde, C. J. H., Putter, H., Smit, V. T. H.  
653 B. M., Liefers, G. J., Kuppen, P. J. K., Tollenaar, R. A. E. M., Mesker, W. E.,  
654 2011. Tumorstroma ratio in the primary tumor is a prognostic factor in early

- 655 breast cancer patients, especially in triple-negative carcinoma patients. *Breast*  
656 *Cancer Research and Treatment* 125 (3), 687696.
- 657 Demir, C., Yener, B., 2009. Automated cancer diagnosis based on histopatholog-  
658 ical images: A systematic survey. Technical Report, Rensselaer Polytechnic  
659 Institute, Department of Computer Science.
- 660 Deng, J., Dong, W., Socher, R., Li, L.-J., Li, K., Fei-Fei, L., 2009. ImageNet: A  
661 Large-Scale Hierarchical Image Database. In: *CVPR09*. pp. 248–255.
- 662 Doyle, S., Feldman, M., Tomaszewski, J., Shih, N., Madabhushi, A., 2011. Cas-  
663 caded multi-class pairwise classifier (CASCAMPA) for normal, cancerous, and  
664 cancer confounder classes in prostate histology. In: *ISBI*. pp. 715–718.
- 665 Everingham, M., Van Gool, L., Williams, C. K. I., Winn, J., Zisserman, A., 2012.  
666 The PASCAL Visual Object Classes Challenge 2012 (VOC2012) Results.
- 667 Fatakdawala, H., Xu, J., Basavanahally, A., Bhanot, G., Ganesan, S., Feldman,  
668 F., Tomaszewski, J., Madabhushi, A., 2010. Expectation-maximization-driven  
669 geodesic active contours with overlap resolution (EMaGACOR): Application to  
670 lymphocyte segmentation on breast cancer histopathology. *IEEE Transactions*  
671 *on Biomedical Engineering* 57 (7), 1676–1690.
- 672 Ghaznavi, F., Evans, A., Madabhushi, A., Feldman, M. D., 2013. Digital imaging  
673 in pathology: Whole-slide imaging and beyond. *Annual Review of Pathology*  
674 *Mechanisms of Disease* 8 (1), 331–359.
- 675 Gurcan, M., Boucheron, L., Can, A., Madabhushi, A., Rajpoot, N., Bulent,  
676 Y., 2009. Histopathological image analysis: a review. *IEEE Transactions on*  
677 *Biomedical Engineering* 2, 147–171.
- 678 Han, J., Chang, H., Loss, L., Zhang, K., Baehner, F., Gray, J., Spellman, P., Parvin,  
679 B., 2011. Comparison of sparse coding and kernel methods for histopathologi-  
680 cal classification of glioblastoma multiforme. In: *ISBI*. pp. 711–714.
- 681 Huang, C., Veillard, A., Lomeine, N., Racoceanu, D., Roux, L., 2011. Time ef-  
682 ficient sparse analysis of histopathological whole slide images. *Computerized*  
683 *medical imaging and graphics* 35 (7-8), 579–591.
- 684 Huang, F. J., LeCun, Y., 2006. Large-scale learning with svm and convolutional  
685 for generic object categorization. In: *Proceedings of the 2006 IEEE Computer*

- 686 Society Conference on Computer Vision and Pattern Recognition - Volume 1.  
687 CVPR '06. IEEE Computer Society, Washington, DC, USA, pp. 284–291.
- 688 Huang, W., Hennrick, K., Drew, S., 2013. A colorful future of quantitative pathol-  
689 ogy: validation of vectra technology using chromogenic multiplexed immuno-  
690 histochemistry and prostate tissue microarrays. *Human Pathology* 44, 29–38.
- 691 Huijbers, A., Tollenaar<sup>1</sup>, R., v Pelt<sup>1</sup>, G., Zeestraten<sup>1</sup>, E., Dutton, S., McConkey,  
692 C., Domingo, E., Smit, V., Midgley, R., Warren, B., Johnstone, E. C., Kerr, D.,  
693 Mesker, W., 2013. The proportion of tumor-stroma as a strong prognosticator  
694 for stage ii and iii colon cancer patients: validation in the victor trial. *Annals of*  
695 *Oncology* 24 (1), 179185.
- 696 Jarrett, K., Kavukcuoglu, K., Ranzato, M., LeCun, Y., 2009. What is the best  
697 multi-stage architecture for object recognition? In: *Proc. International Confer-*  
698 *ence on Computer Vision (ICCV'09)*. IEEE, pp. 2146–2153.
- 699 Jia, Y., Shelhamer, E., Donahue, J., Karayev, S., Long, J., Girshick, R., Guadar-  
700 rama, S., Darrell, T., 2014. Caffe: Convolutional architecture for fast feature  
701 embedding. *arXiv preprint arXiv:1408.5093*.
- 702 Kavukcuoglu, K., Ranzato, M., LeCun, Y., 2008. Fast inference in sparse coding  
703 algorithms with applications to object recognition. *Tech. Rep. CBLL-TR-2008-*  
704 *12-01*, Computational and Biological Learning Lab, Courant Institute, NYU.
- 705 Kong, J., Cooper, L., Sharma, A., Kurk, T., Brat, D., Saltz, J., 2010. Texture based  
706 image recognition in microscopy images of diffuse gliomas with multi-class  
707 gentle boosting mechanism. In: *ICASSAP*. pp. 457–460.
- 708 Kothari, S., Phan, J., Osunkoya, A., Wang, M., 2012. Biological interpretation  
709 of morphological patterns in histopathological whole slide images. In: *ACM*  
710 *Conference on Bioinformatics, Computational Biology and Biomedicine*. pp.  
711 218–225.
- 712 Krizhevsky, A., Sutskever, I., Hinton, G. E., 2012. Imagenet classification with  
713 deep convolutional neural networks. In: *Advances in Neural Information Process-*  
714 *ing Systems 25: 26th Annual Conference on Neural Information Process-*  
715 *ing Systems 2012. Proceedings of a meeting held December 3-6, 2012, Lake*  
716 *Tahoe, Nevada, United States*. pp. 1106–1114.

- 717 Lan, C., Heindl, A., Huang, X., Xi, S., Banerjee, S., Liu, J., Yuan, Y., 2015. Quan-  
718 titative histology analysis of the ovarian tumour microenvironment. *Scientific*  
719 *Reports* 5 (16317).
- 720 Lazebnik, S., Schmid, C., Ponce, J., 2006. Beyond bags of features: Spatial pyra-  
721 mid matching for recognizing natural scene categories. In: *Proceedings of the*  
722 *Conference on Computer Vision and Pattern Recognition*. pp. 2169–2178.
- 723 Le, Q., Han, J., Gray, J., Spellman, P., Borowsky, A., Parvin, B., 2012. Learning  
724 invariant features from tumor signature. In: *ISBI*. pp. 302–305.
- 725 Lecun, Y., Bottou, L., Bengio, Y., Haffner, P., 1998. Gradient-based learning ap-  
726 plied to document recognition. In: *Proceedings of the IEEE*. pp. 2278–2324.
- 727 Lee, H., Battle, A., Raina, R., Ng, A. Y., 2007. Efficient sparse coding algorithms.  
728 In: *In NIPS*. *NIPS*, pp. 801–808.
- 729 Levenson, R. M., Borowsky, A. D., Angelo, M., 2015. Immunohistochemistry and  
730 mass spectrometry for highly multiplexed cellular molecular imaging. *Labora-*  
731 *tory Investigation* 95, 397–405.
- 732 Mairal, J., Bach, F., Ponce, J., Sapiro, G., Mar. 2010. Online learning for matrix  
733 factorization and sparse coding. *J. Mach. Learn. Res.* 11, 19–60.
- 734 Nayak, N., Chang, H., Borowsky, A., Spellman, P., Parvin, B., 2013. Classifi-  
735 cation of tumor histopathology via sparse feature learning. In: *Proc. ISBI*. pp.  
736 410–413.
- 737 Rimm, D. L., 2014. Next-gen immunohistochemistry. *Nature Methods* 11, 381–  
738 383.
- 739 Rogojanu, R., Thalhammer, T., Thiem, U., Heindl, A., Mesteri, I., Seewald, A.,  
740 Jger, W., Smochina, C., Ellinger, I., Bises, G., 2015. Quantitative image anal-  
741 ysis of epithelial and stromal area in histological sections of colorectal cancer:  
742 An emerging diagnostic tool. *BioMed Research International* 2015 (569071),  
743 179185.
- 744 Serre, T., Wolf, L., Poggio, T., 2005. Object recognition with features inspired  
745 by visual cortex. In: *Proceedings of the Conference on Computer Vision and*  
746 *Pattern Recognition*. Vol. 2. pp. 994–1000.



- 747 Stack, E. C., Wang, C., Roman, K. A., Hoyt, C. C., 2014. Multiplexed immuno-  
748 histochemistry, imaging, and quantitation: A review, with an assessment of  
749 tyramide signal amplification, multispectral imaging and multiplex analysis.  
750 *Methods* 70 (1), 46–58.
- 751 Tropp, J., Gilbert, A., 2007. Signal recovery from random measurements via or-  
752 thogonal matching pursuit. *Information Theory, IEEE Transactions on* 53 (12),  
753 4655–4666.
- 754 Vedaldi, A., Zisserman, A., 2012. Efficient additive kernels via explicit feature  
755 maps. *IEEE Transactions on Pattern Analysis and Machine Intelligence* 34 (3),  
756 480–492.
- 757 Wang, J., Yang, J., Yu, K., Lv, F., Huang, T., Gong, Y., 2010. Locality-constrained  
758 linear coding for image classification. In: *Proceedings of the Conference on*  
759 *Computer Vision and Pattern Recognition*. pp. 3360–3367.
- 760 Wu, R., Yu, Y., Wang, W., 2013. Scale: Supervised and cascaded laplacian eigen-  
761 maps for visual object recognition based on nearest neighbors. In: *CVPR*. pp.  
762 867–874.
- 763 Yang, J., Yu, K., Gong, Y., Huang, T., 2009. Linear spatial pyramid matching  
764 using sparse coding for image classification. In: *Proceedings of the Conference*  
765 *on Computer Vision and Pattern Recognition*. pp. 1794–1801.
- 766 Yosinski, J., Clune, J., Bengio, Y., Lipson, H., 2014. How transferable are features  
767 in deep neural networks? In: *Advances in Neural Information Processing Sys-*  
768 *tems 27: Annual Conference on Neural Information Processing Systems 2014,*  
769 *December 8-13 2014, Montreal, Quebec, Canada*. pp. 3320–3328.
- 770 Young, R. A., Lesperance, R. M., 2001. The gaussian derivative model for spatial-  
771 temporal vision. I. Cortical Model. *Spatial Vision* 2001, 3–4.
- 772 Zheng, M., Bu, J., Chen, C., Wang, C., Zhang, L., Qiu, G., Cai, D., 2011. Graph  
773 regularized sparse coding for image representation. *IEEE Transactions on Im-*  
774 *age Processing* 20 (5), 1327–1336.
- 775 Zhou, Y., Barner, K. E., 2013. Locality constrained dictionary learning for non-  
776 linear dimensionality reduction. *IEEE Signal Process. Lett.* 20 (4), 335–338.

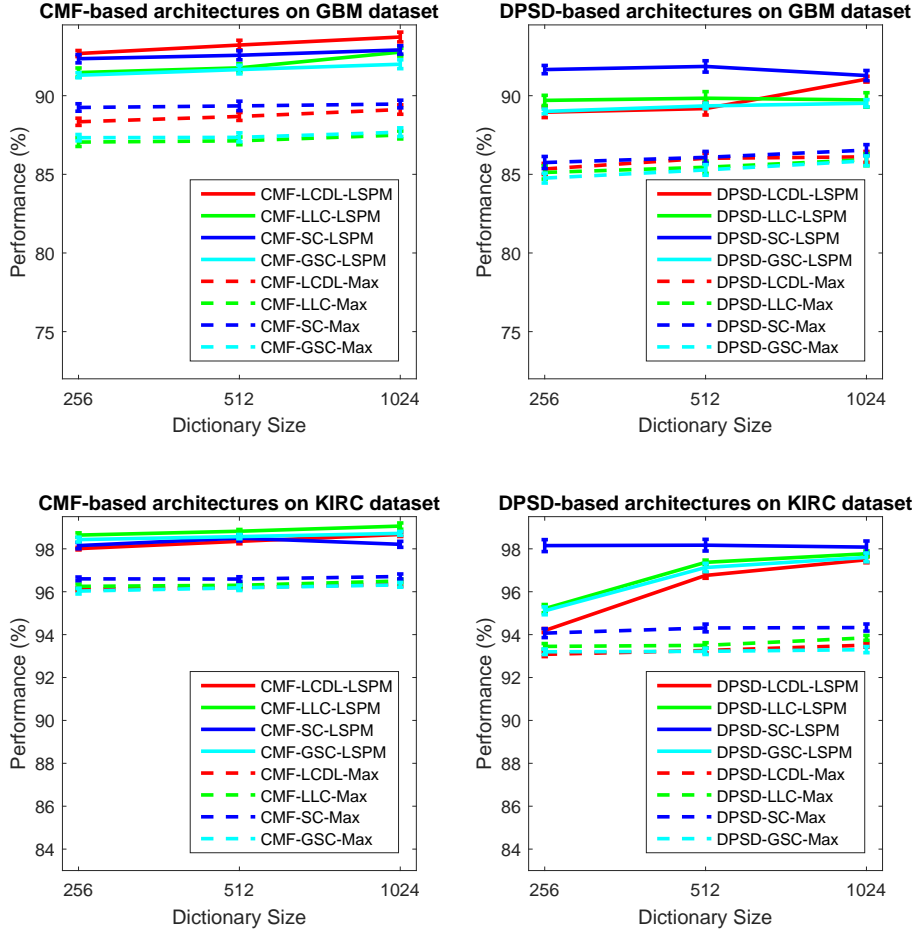


Figure 9: Evaluation of the impact of different spatial pooling strategies with the **FE-SFE-LSPM** framework on both GBM and KIRC datasets. Note that, given many of the popular spatial pooling strategies, *max* pooling is chosen due to the extensive justification by both biophysical evidence in the visual cortex and researches in image categorization tasks. The derived architecture is described as **FE-SFE-Max**, and only the top-two-ranked features (i.e., DPSD and CMF) are involved during evaluation. Here, the performance is reported as the mean and standard error of the correct classification rate, as detailed in Section 4.

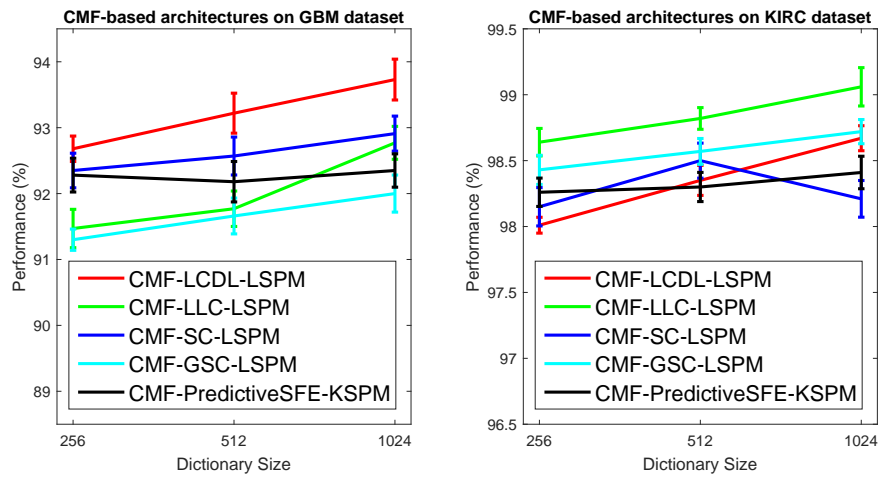


Figure 10: Systems built-upon CMF-**PredictiveSFE** provide very competitive performance compared to systems built-upon CMF-**SFE**. Here, the performance is reported as the mean and standard error of the correct classification rate, as detailed in Section 4.